Contents lists available at ScienceDirect

Energy Storage Materials

journal homepage: http://ees.elsevier.com

A high-performance lithium-ion capacitor with carbonized $NiCo_2O_4$ anode and vertically-aligned carbon nanoflakes cathode

Chung-Fu Cheng[a], Xiang Li[a], Kewei Liu[a], Feng Zou[a], Wei-Yao Tung[a], Yi-Fan Huang[a,b], Xuhui Xia[c], Chien-Lung Wang[b], Bryan D. Vogt[c], Yu Zhu[a,*]

[a] Department of Polymer Science, University of Akron, OH, 44308, USA
[b] Department of Applied Chemistry, National Chiao Tung University, Hsinchu, 30010, Taiwan
[c] Department of Polymer Engineering, University of Akron, OH, 44308, USA

ARTICLE INFO

Keywords
Lithium ion capacitor
Vertically aligned carbon nanoflakes
Metal-organic frameworks
Energy storage

ABSTRACT

Lithium ion capacitors (LICs) are energy storage devices integrating the complementary features of both supercapacitors and lithium ion batteries to reach high energy and power densities. One of major challenges in LIC technology is the kinetic imbalance between the faradaic insertion anode and capacitive cathode. Therefore, the design of electrode materials is crucial to enhance the ratability of anode and the capacitance of cathode in LIC devices. In this work, novel LICs were demonstrated with nanostructural cathode and anode. A vertically-aligned carbon nanoflakes (VACNFs) cathode provided high electrochemically active surface area and excellent conductivity, while a metal organic frameworks (MOFs) derived carbonized nickel cobalt oxide ($cNiCo_2O_4$) anode ensured fast conversion reactions and remarkable cyclability. Electrochemical characterizations of individual electrode confirmed that both electrodes exhibited good electron and ion transport capability. The LICs were fabricated with optimized electrode active materials loading to deliver high energy densities at desired charge/discharge rates. The devices exhibited an energy density up to 136.9 W h/kg (at 200 W/kg). At higher power density of 40 kW/kg, under which a full charge-discharge can be finished within 4 s, the LICs could still deliver an energy density of 26.44 W h/kg. The devices also showed a good cycle stability (≈90% capacitance retention after 9000 cycles, under current density of 4 A/g) within the voltage range of 1–4.2 V.

1. Introduction

With the rapid growth of the market for portable electronics and electric vehicles, as well as the expanding utilization of renewable energy, the development of new energy storage devices with high power and energy densities becomes paramount importance [1,2]. Among electrochemical energy storage technologies, lithium-ion batteries (LIBs) and supercapacitors (SCs) have been active topics for both research and commercialization in the past decades [3–6]. Although LIBs and SCs have similar device structure with laminated porous electrodes, porous separators, and liquid electrolytes, their charge-storage mechanisms are distinctly different. LIBs exhibit high energy density (150–250 W h/kg) owing to intercalation mechanism which delivers high specific capacity. However, the sluggish solid-state ion diffusion in bulk electrodes also limits their power density (typically <1 kw/kg) and cyclability (typically ~1000 cycle) [7,8]. On the contrary, SCs provide high power density (typically >10 kw/kg) and cyclability (typically >10000 cycle) by fast physical absorption/desorption of electrolyte ions at the interface of electrode and electrolyte. As the charge accumulation on the interface is limited by the surface area, the energy densities of SCs are usually low [9–12]. However, the applications of electrochemical energy storage devices have varied requirements on energy density and power density, which lead to the development of new devices with balanced energy storage performance.

Recently, Li-ion capacitors (LICs) have emerged as a new type of electrochemical energy storage devices that fill the gap between LIBs and SCs by providing balanced high specific energy and power [13–15]. A LIC system is generally composed of a highly porous SC-like carbon cathode, a LIB-like intercalation anode and organic electrolytes with Li salts. With the doping of lithium ion at the anode, the cell voltage of LIC could be operated around 4 V, which is significantly higher than commercial SCs operated at 2.7 V. Therefore, LICs are expected to achieve better energy density than SCs while maintaining similar high power density. Such a unique characteristic renders LICs an advanced energy storage device for applications where high energy density and capacitor-like cyclability are required [16–24]. Because the kinetic rate for intercalation on the anode is slower than the rate of physical adsorption/desorption of solvated ions on the cathode [25], the challenge of LIC is to design the materials that could solve the kinetic imbalance between the cathode and the anode.

* Corresponding author.
Email address: yu.zhu@uakron.edu (Y. Zhu)

https://doi.org/10.1016/j.ensm.2019.07.034
Received 18 Febraury 2019; Received in revised form 17 July 2019; Accepted 20 July 2019
Available online xxx
2405-8297/

Accordingly, introduction of both appropriate anode and cathode materials to achieve synergy in transport and electrochemical properties becomes imperative in LICs. Currently, most LIC anodes are intercalation electrodes, such as graphite, MoS_2 or TiO_2, which have sluggish intercalation rate and relatively low specific capacities [26,27]. A straightforward route to improve the performance of LICs is to introduce anode materials with higher ratability and specific capacity. It is notable that some anode materials such as VN and TiC with well-defined nanostructure, have been extensively used in LIC systems because their fast Li^+ diffusion kinetics could further overcome the kinetic imbalance of the slow faradaic insertion anode and the fast capacitive cathode [19,28]. Recently, conversion reaction mechanism-based transition metal oxides such as Nb_2O_5, and Fe_3O_4 [3,16,29], have been explored as alternative high specific capacity, high rate anodes for LICs. In those researches, a well-defined nanostructural anode material is the key to obtain stable cycling performance. On the cathode side, the major limitation is the low specific capacitance of conventional activated carbon. Although the activated carbon has significant surface area, the unconnected carbon particles lead to a low electrochemically active surface area, which restrains the electron/ion transport during charge/discharge cycle [30]. Furthermore, based on the capacitance equation ($\frac{1}{C_{LIC}} = \frac{1}{C_{Anode}} + \frac{1}{C_{Cathode}}$) [31], the low specific capacitance of the cathode will significantly decrease the specific capacitance of overall the LICs device, resulting in the low energy density. Therefore, the development of the cathode materials with larger electrochemically active surface areas and high conductivity should be emphasized.

Based on the above comprehensive considerations, an integrated LIC with bimetallic oxide conversion anode and the vertically aligned carbon nanoflakes cathode was developed in this work (Fig. 1). The metal organic framework (MOF) derived metal oxide composites were used to form anode materials. This method has been proved in previous studies [32–35] to produce stable conversion anode in different secondary batteries. In this study, the carbonized $NiCo_2O_4$ ($cNiCo_2O_4$) nanocomposites with unique rhombic dodecahedron morphology were obtained by multi-stage thermal treatments from NiCo-MOFs precursor materials. The $cNiCo_2O_4$ nanocomposites, owing to their high surface areas and high pseudocapacitance from conversion reaction, exhibited large Li-ion storage capability and good charge/discharge rate as an anode material. The cathode materials, vertically aligned carbon nanoflakes (VACNFs), was synthesized by chemical vapor deposition technique on the current collector. This binder-free VACNFs cathode material exhibited several favorable characteristics such as excellent intrinsic conductivity, high specific surface area and large accessible electrochemically active surface, which ameliorate the inaccessibility of ions in the organic electrolyte. After the integration of these high-performance electrodes, the assembled VACNFs and $cNiCo_2O_4$ nanocomposites LICs demonstrated outstanding energy density (~136.9 W h/kg at 200 W/kg) and power density (~40 kW/kg at 26.44 W h/kg). This result demonstrated that the high performance LICs could be achieved by well-designed nanostructural electrode materials.

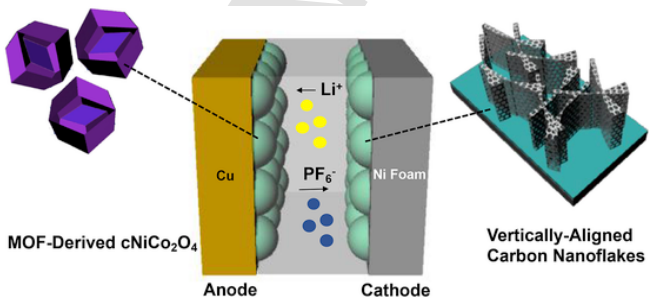

Fig. 1. Schematic illustration for the design of the Li-ion capacitor.

2. Materials and methods

2.1. Preparation of NiCo MOF

The detailed procedure of the fabrication of NiCo MOF is reported in the published work [36,37]. In brief, $Ni(NO_3)_2{\cdot}6H_2O$ (582 mg, 2 mmol) and $Co(NO_3)_2{\cdot}6H_2O$ (1164 mg, 4 mmol) were dissolved in methanol (MeOH) (60 mL) to form a clear solution. Then this solution was gradually poured into MeOH (20 mL) containing 2-methylimidazole (1968 mg, 24 mmol). The mixture was heated at 150 °C for 12 h, allowing the formation of NiCo MOF structure through a self-assembly process. The reaction mixture was washed with methanol for several times and the solid phase was separated by centrifugation. The product purple powder was obtained after drying in oven at 100 °C.

2.2. Preparation of $cNiCo_2O_4$ nanocomposite

To produce $cNiCo_2O_4$ nanocomposites, the NiCo MOF was annealed at 250 °C in air with ramping rate about 1 °C/min for 1 h to remove liquid impurities and residue solvents. After this step, the carbonization reaction was performed to form the carbon coated materials. The sample was placed in a tube furnace and the temperature was increased to 450 °C with ramping rate about 5 °C/min and kept for 1 h. The sample was then cooled down to room temperature. The carbonization process was carried out under Argon atmosphere. Finally, the carbonized sample was collected and annealed in air at 300 °C for 5 h to oxidize the Ni and Co, forming $cNiCo_2O_4$ nanocomposites.

2.3. Preparation of VACNFs

To form the catalyst on the top of Ni-foam, Al_2O_3 and Fe were deposited by electron-beam evaporator (Denton vacuum DV-502 A and Denton vacuum deg-2 minigun modified). 10 nm of Al_2O_3 was deposited as the buffer layer, and then 1 nm Fe was deposited as the catalysts for the VACNFs growth. VACNFs were grown using a self-assembled chemical vapor deposition system under 1 atm condition. The coated Ni-foam sample was placed in the cold zone of the tub furnace with a magnetic loading boat. Argon (5.0 UHP grade 99.999%, Praxair) was purged into the CVD system with the vacuum pump running to ensure the inert atmosphere inside the tube. Then, hydrogen (5.0 UHP grade 99.999%, Praxair, 100 sccm) was introduced and Argon was closed. The vacuum pump was closed shortly after Argon was closed. The purging hydrogen was filling up the tube and the vacuum level of the CVD system was monitored by barometers. Once the pressure reached 1 atm, a switch valve was opened to connect the downstream of CVD system to the exhausting line. The hydrogen atmospheric pressure was maintained during the growth. When the furnace reached 800 °C, the sample was hot-loaded into the center of the tube furnace. At the same time, water vapor (bubbled by 50 sccm hydrogen) was introduced to the tube. The annealing time was 5 min. After annealing, ethylene (2.5 Grade 99.5%, Praxair) was introduced into the reaction chamber (80 sccm) to grow the VACNFs. The growth time was 10 min. After the growth, the carbon source was immediately closed and the sample was loaded to the cold zone. Then Argon was introduced to replace the hydrogen and fill the furnace. The samples were taken out when the furnace temperature was close to room temperature.

2.4. Electrodes activation and LIC device fabrication

The anode materials were mixed with carbon black and poly(acrylic acid) (PAA) at a ratio of 7 : 2: 1, respectively. NMP was added to this mixture and all materials were subsequently mixed by pestle and mor-

tar to produce homogenous slurries. The anode slurries were casted on a copper foil using a doctor blade. The casted electrodes were placed in an oven at 50 °C overnight to remove the residual solvent. For the cathode material, the VACNFs on Ni foam were directly used as binder-free cathode. 2032 coin cells were used for the fabrication of all half cells and LIC devices. Lithium foil was used as counter electrode in half-cells. The fabrication of the cells was conducted in an Ar filled glovebox. Celgard 2400 was used as the separator. The electrolyte was 1 M lithium hexafluorophosphate solution in EC and DEC (1:1 v/v). The electrode was punched into 5/16-inch circular discs. The typical mass loading was 0.4–0.6 mg/cm^2 for the anode and 1.6–2.4 mg/cm^2 for the cathode. Before the testing of the full LIC device, the anode materials were prelithiated by using Li reference electrode for charging/discharging under low current density (0.1 A/g) for 10 cycles.

3. Results and discussions

3.1. Anode material characterization

The precursor bimetallic MOF (NiCo MOF) was prepared by solvothermal methods with 2-methylimidazole and divalent Ni and Co ions in a methanol solution [36,37]. The detailed procedure is described in the experimental section. The morphology of the NiCo MOF was characterized by scanning electron microscopy (SEM) and transmission electron microscopy (TEM) as shown in Fig. 2 (a,b), respectively. Compared to the reported Ni or Co single metallic MOFs [38,39], similar rhombic dodecahedron nanoparticles with a uniform particle size of ≈400 nm could be clearly observed. Furthermore, the selected area electron diffraction (SAED) also confirmed the initial formation of the amorphous nanoparticles (Fig. S1).

To convert the NiCo MOF into electrochemically active carbonized $NiCo_2O_4$ ($cNiCo_2O_4$), a series of thermal treatments were carried out. In the first stage, low temperature calcination (250 °C) was performed in air to remove residue solvent and other impurities from solvothermal reaction. The corresponding TEM micrograph (Fig. S2(a)) confirmed the preservation of the nanostructure after the first-stage calcination. Subsequently, the carbonization reaction was conducted at 450 °C under Argon to form the carbon coating and convert the Ni/Co ions into corresponding metallic form. As demonstrated in Fig. S2(b), the nanostructure could be well reserved after carbonization reaction. In the final step, the sample was further annealed in air at 300 °C to oxidize the Ni and Co, forming $cNiCo_2O_4$. As shown by the TEM and SEM micrographs in Fig. 2(c and d), the nanostructure of the $cNiCo_2O_4$ nanocomposite was retained after the series of thermal treatments as compared with Fig. 2 (a,b), suggesting the successful preparation of the bimetallic oxide with well-defined nanostructure.

Selected area electron diffraction (SAED) and wide-angle X-ray diffraction (WAXD) were used to characterize $cNiCo_2O_4$ nanocomposite. Fig. 2(e) displays the SAED pattern of the $cNiCo_2O_4$ nanocomposite. Note that all the rings can be indexed with the face centered cubic (fcc) $cNiCo_2O_4$ nanocomposite. The WAXD results of the $cNiCo_2O_4$ nanocomposite (Fig. 2(f)) are in line with the SAED results. All the diffractions can be indexed as fcc $NiCo_2O_4$ (JCPDS card no. 73–1702) with the lattice constant a = 8.114 Å. High-resolution TEM (HRTEM) was utilized to directly visualize the crystalline lattice in real space. Fig. 2(g) displays the lattice fringes of $cNiCo_2O_4$ nanocomposite. The (111) and the (200) planes of $cNiCo_2O_4$ (Fig. 2(g)) are consistent with the calculated results from XRD (Fig. 2(f)). To confirm the elemental distribution of C, Ni and Co, energy dispersive X-ray spectroscopy (EDS) mapping was further performed. As demonstrated in Fig. 2 (h,i,j,k), the three selected elements (carbon, nickel and cobalt) were uniformly distributed in each particle without elemental aggregation or significant gradient separation. The carbon content in the $cNiCo_2O_4$ nanocomposite was quantitatively analyzed by thermogravimetric analysis (TGA) in Fig. S3. The TGA results indicated the composition of the carbon content in the $cNiCo_2O_4$ was ~20%. Furthermore, Brunauer–Emmett–Teller (BET) tests were conducted to measure the specific surface area. According to the BET analysis shown in Fig. S4(a), $cNiCo_2O_4$ with well-defined nanostructure, that is, rhombic dodecahedron like nanoparticles, exhibits high specific surface area about 263 m^2/g. The porosity of $cNiCo_2O_4$ is 12.8%. It is worth to note that

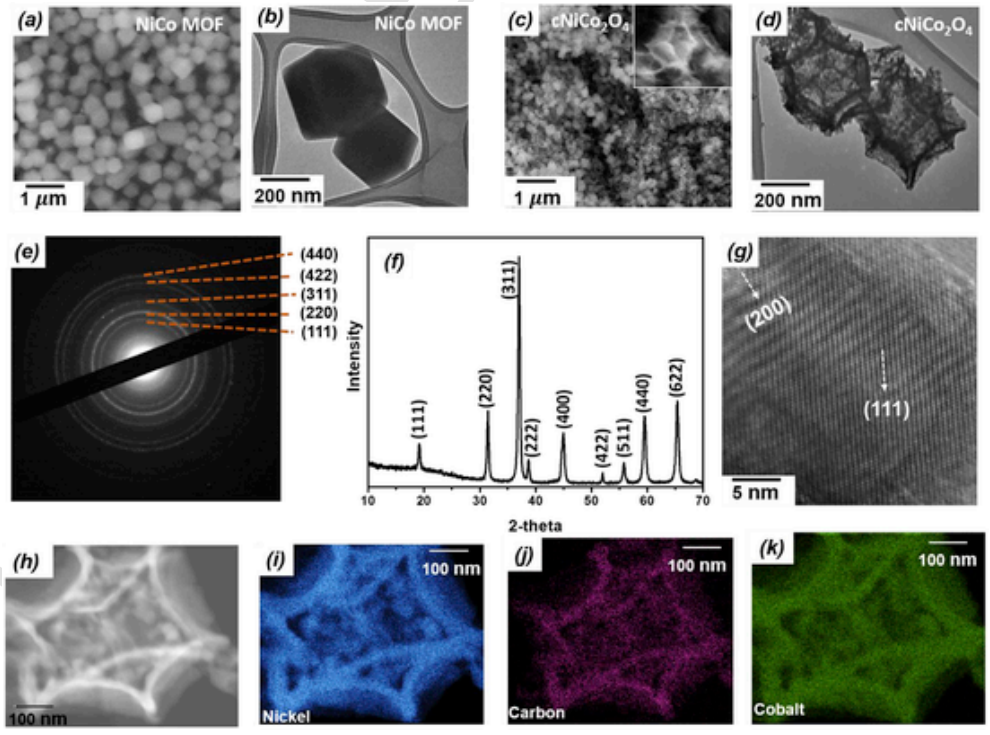

Fig. 2. (a) SEM micrograph of NiCo MOF, (b) TEM micrograph of NiCo MOF, (c) SEM micrograph of $cNiCo_2O_4$ nanocomposite, (d) TEM micrograph of $cNiCo_2O_4$ nanocomposite, (e) SAED pattern of $cNiCo_2O_4$ nanocomposite, (f) WAXD profile of $cNiCo_2O_4$ nanocomposite, (g) HRTEM micrograph of $cNiCo_2O_4$ nanocomposite. (h,i,j,k) Elemental mapping images of the $cNiCo_2O_4$ nanocomposite.

the surface area could be controlled by the nanostructure and particle size. The control of the thermal treatment is the key to preserve the nanostructure. The TEM micrographs of samples with different thermal treatment were shown in Figs. S13a and S13b. With the increase of the temperature ramping rate (20 °C/min) or using higher final temperature (600 °C), the nanostructure of $cNiCo_2O_4$ would collapse and deform. The results were further confirmed by specific surface area (curve a and b) in Fig. S13 (d). The specific surface area could drop to 72 and 12 m^2/g, respectively.

3.2. Electrochemical properties of the anode

To systematically characterize the electrochemical properties of $cNiCo_2O_4$ nanocomposite, half-cell tests using a $cNiCo_2O_4$ nanocomposite electrode and a lithium metal counter electrode were performed. Cyclic voltammetry (CV) measurements at various scan rates were performed to understand the redox processes occurring in the as-prepared $cNiCo_2O_4$ electrode. Based on reported conversion reaction mechanism of several transition metal oxides, Li insertion and extraction reactions in the $NiCo_2O_4$ nanocomposites could be expressed as follows:

$$NiCo_2O_4 + 8Li^+ + 8e^- \leftrightarrow Ni + 2Co + 4Li_2O \quad (1)$$

Generally, the storage mechanism can be revealed by the dependence of the peak current (i) on the scan rate (v) as [39].

$$i = av^b \quad (2)$$

where a and b are adjustable variables. b = 0.5 indicates a semi-infinite diffusion process, and b = 1 indicates a capacitive process [40]. The value of slope b is usually obtained by plotting log i versus log ν. Accordingly, the current i at a given voltage is the sum of two contributions arising from the redox pseudocapacitance and diffusion capacity as described below.

$$i = a_1 v + a_2 v^{1/2} \quad (3)$$

where $a_1\nu$ and $a_2\nu^{1/2}$ correspond to the current contributions from the capacitive and diffusion processes, respectively [40]. As shown in Fig. 3(a), a linear relationship is observed between the peak current and the scan rate with slope of 0.63 and 0.64 for the charge and discharge curves, respectively. The results suggested that both diffusion and capacitive processes in the scan rate ranging from 1 mV/s to 10 mV/s are incorporated during charging and discharging. The total current could be derived from the contribution of capacitive and diffusive processes as shown in Fig. 3(b) (scan rate of 2 mV/s). The pseudo-capacitive properties of the $cNiCo_2O_4$ nanocomposite was further confirmed by the increasing of the CV scan rate as shown in Fig. S5. The redox peaks are significantly reduced as compared with the low rate CV, indicating the dominate pseudo-capacitive behavior at higher scan rate.

The $cNiCo_2O_4$ nanocomposite electrodes also exhibited an impressive rate capability. The rate performance of the cell at current densities from 0.5 A/g to 20 A/g, each run for 10 cycles prior to the continuation of the next step at a higher rate, exhibited reversible specific capacities as shown in Fig. 3(c). The discharge specific capacities are 1192, 1066, 869, 756, 589 and 392 mA h/g at 0.5, 1, 2, 5, 10 A/g and 20 A/g, respectively. Notably, the capacity of the electrode can recover to original values when the current density is set back to 2 A/g and 0.5 A/g. The galvanostatic charge/discharge curves with current densities ranging from 0.5 to 20 A/g are presented in Fig. S6. The excellent ratability of the $cNiCo_2O_4$ nanocomposite could be associated to its hierarchical structure with uniform carbon coating, which improved the transport of both lithium ions and electrons.

Long cycle galvanostatic charge and discharge experiments were conducted to investigate the cycle stability of the electrode. The half-cell was initiated at 0.2 A/g for the four-cycles and then cycled at 2 A/g within the voltage window of 0.02–3.0 V. As shown in Fig. 3 (d), the $cNiCo_2O_4$ nanocomposite electrode shows excellent cycling stability with the capacity steadily maintained at ~ 853 mA h/g after 500 cycles. The capacity slightly decreased to 792 mA h/g after 900 cycles and the corresponding fading rate was about 0.013% per cycle. As expected, with the unique rhombic dodecahedron nanostructure, these $cNiCo_2O_4$

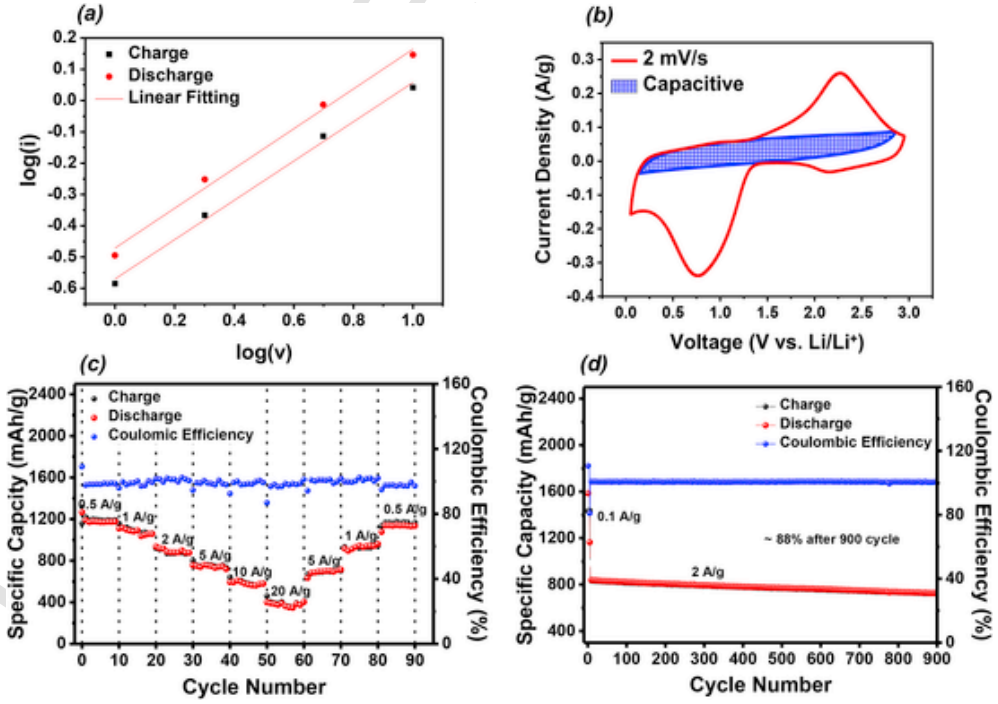

Fig. 3. Electrochemical characterization of $cNiCo_2O_4$ nanocomposite electrode (a) The power law relationship of charge/discharge peak current and scan rate (1–10 mV/s). (b) CV curve of the $cNiCo_2O_4$ nanocomposite electrode with scan rate of 2 mV/s. The capacitive portion is shown in the shadowed area. (c) Rate performance at different current densities ranging from 0.5 to 20 A/g. (d) Cyclic performance of the $cNiCo_2O_4$ nanocomposite electrode at 2 A/g up to 900 cycles.

nanocomposite anodes exhibited high specific capacity and long-term cycling stability. The electrochemical impedance spectra of the $cNiCo_2O_4$ electrode after different charge/discharge cycles was recorded as shown in Fig. S7(a). From those spectra, the capacitor-like behavior can be further confirmed by the vertical slopes in the low frequency region, indicating the fast diffusion of the electrolyte. The decrease of the charge-transfer resistance (R_{ct}) with increasing charge/discharge cycle is in accordance with reported literatures using metal oxide-based electrode [41,42] (See Table S1 for details), which was usually attributed to the activation process during cycles [43]. It is worth to mention that $cNiCo_2O_4$ also exhibited lower charge transfer resistance than pure $NiCo_2O_4$ (Fig. S7c). We speculate that the low charge transfer resistance of $cNiCo_2O_4$ could be attributed to the uniform distribution of carbon in $cNiCo_2O_4$ nanoparticles.

3.3. Cathode material characterization

To develop high-performance carbon-based cathode materials in LICs, it is essential to prepare carbon-based nanomaterials with high surface area and conductivity. Nanoporous carbon with well-defined structure, such as carbon nanosheets or carbon nanoflakes, are considered as promising candidates due to their high electronic conductivity, large specific surface area, and flexibility for the host of different functional materials [44–47]. For instance, a highly porous graphene nanosheet with vertical orientation was prepared by radio frequency plasma enhanced chemical vapor deposition, and was reported to increase the specific capacitance in the supercapacitor [48]. Herein, vertically aligned carbon nanoflakes (VACNFs) on Ni-foam was fabricated by thermal chemical vapor deposition (CVD) and was used as binder-free cathodes. As shown in Fig. 4(a), Fe and Al_2O_3 were deposited on the Ni-foam as catalyst and buffer layers, respectively. Subsequently, ethylene was used as the carbon source to grow VACNFs (see experimental part for the details). The SEM images shown in Fig. 4(b-d) depict the morphologies of the VACNFs on Ni-foam under different magnifications. As verified by Fig. 4(b), the VACNFs were uniformly distributed on the frameworks of the Ni-foam. Fig. 4(c) and d shows the detailed morphologies of the VACNFs under higher magnification, suggesting the well alignment of the carbon nanoflakes alone the perpendicular orientation from the Ni foam surface. The corresponding TEM image is shown in Fig. 4(e), indicating the height of an individual carbon nanoflake about 3 μm. Selected area electron diffraction was carried out to characterize the graphitic structure of the carbon nanoflakes. As shown in Fig. 3(f), the hexagonal diffraction spots confirm the formation of the sp^2 carbon [48]. HRTEM (High-resolution TEM) was further utilized to evidently reveal the graphitic carbon structure in real space. As shown in Fig. 3(g), the lattice fringes indicate the atomic packing of the graphitic carbon. The Raman spectrum of VACNFs is shown in Fig. S8 and the characteristic D, G, and 2D peaks were observed at 1350, 1580, and 2680 cm^{-1} with a D/G ratio of 0.4 [49]. Furthermore, as shown in Fig. S4(b), the BET analysis of the N_2 adsorption isotherm indicated a high specific surface area of 1152 m^2/g for VACNF, with a porosity of 20.7%. Similar as the synthe-

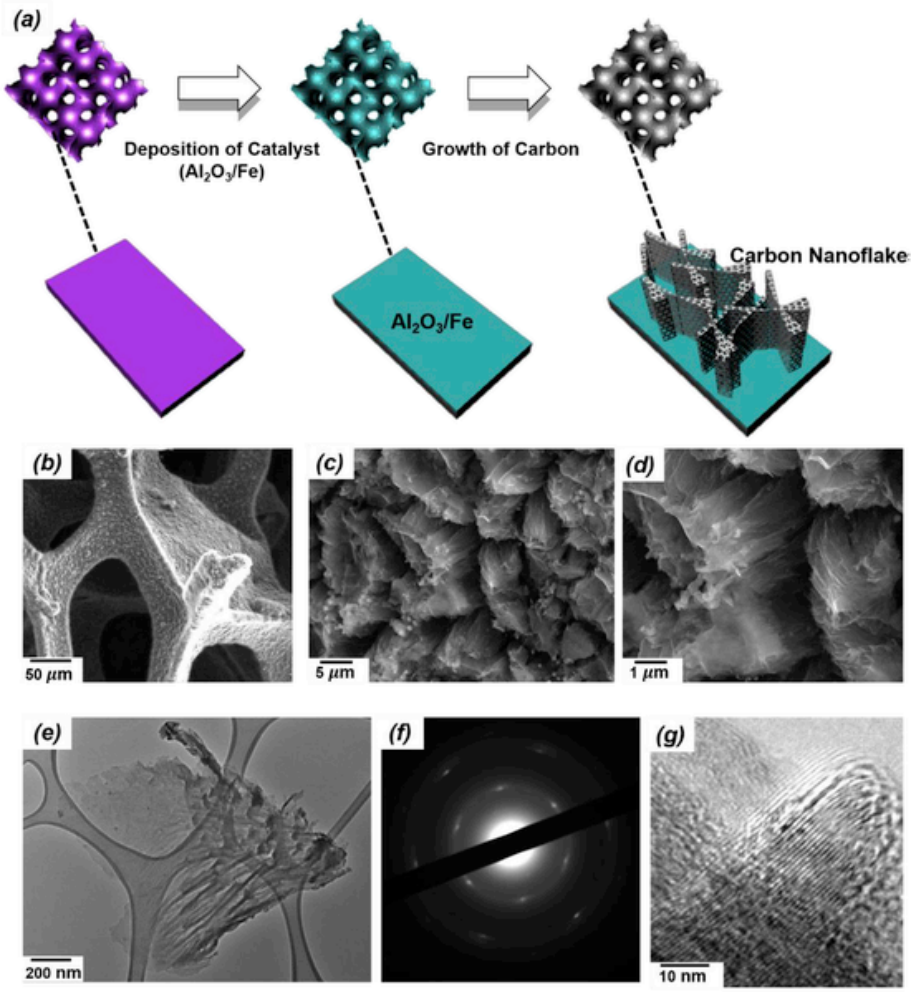

Fig. 4. (a) Schematic diagram of the preparation of VACNFs. (b–d) FESEM micrographs of the VACNFs on Ni-foam with different magnification. (e) TEM micrograph of the VACNFs. (f) SAED pattern of the VACNFs. (g) HRTEM micrograph of the VACNFs.

sis of cathode material, the reaction condition of CVD could significantly affect the morphology and surface area of anode material VACNF. The higher concentration of the carbon feedstock would enhance the formation of amorphous carbon during the deposition, then suppress the vertically-aligned nanostructure. As shown in Fig. S13c, the higher concentration of the carbon source results in the thick amorphous carbon layer on the sample surface, leading to a reduce BET specific surface area of 332 m^2/g (curve c in Fig. S13e).

3.4. Electrochemical properties of the cathode

The electrochemical properties of the VACNFs electrode in a Li half-cell system were characterized by CV and galvanostatic charge/discharge measurements within the voltage range of 2.5–3.9 V versus Li/Li^+ as shown in Fig. 5. The CV curves of the VACNFs electrodes reveal quasi-rectangular shapes at all scan rates, suggesting the dominance of capacitive behavior for these electrodes under all scan rates. Linear galvanostatic charge/discharge curves, which indicated capacitive behavior of the absorption/desorption of anion on the surface of the VACNFs electrode (Fig. S7), were observed and consistent with the CV curves. Owing to the high porosity and conductivity, the VACNFs electrode showed a specific capacity of ≈98.85 mA h/g at 0.5 A/g, and maintained a specific capacity of ≈59.95 mA h/g at 40 times higher current density (at 20 A/g). The half-cell also exhibited an excellent cycling stability (≈97% capacity retention after 900 cycles) (Fig. 5(c)). These properties of VACNFs are superior to those reported for activated carbons (ACs) or other nanocarbons (30–60 mA h/g at 0.1–0.3 A/g) for LICs [50,51]. As shown in Fig. S7(b), Nyquist plots of cathode material showed a broad semicircle at frequencies above 10 Hz for the charge-transfer kinetic-controlled region and a straight line at frequencies below 10 Hz for the mass-transfer-controlled region. Note that the decrease of the R_{ct} with increasing charge/discharge cycle is in line with some reported literatures with carbon-based nanomaterials [52,53]. (See Table S2 for details).

3.5. Lithium ion capacitor

The hybrid LIC was further prepared by integrating $cNiCo_2O_4$ nanocomposites as anode and VACNFs as cathode with 1 M $LiPF_6$ in EC/DEC as electrolyte solution (denoted as VACNFs|$cNiCo_2O_4$). Before the testing of the full LIC device, the anode materials ($cNiCo_2O_4$ nanocomposites) were activated by using Li reference electrode for charging/discharging under low current density (0.1 A/g) for 10 cycles to prelithiate the anode. The mass loading ratio of anode and cathode was 1:3 to optimize the performance by balancing the cathode and anode as determined by half-cell tests. As confirmed by the CV measurement shown in Fig. 6(a), the VACNFs|$cNiCo_2O_4$ LIC device can achieve a high working voltage of 4.2 V. Typical galvanostatic charge–discharge curves of this device at different voltage window are given in Fig. 6(b) (at a fixed current density of 5 A/g). It is notable that the discharge time increased greatly with the increase in the operating voltage window from 3.6 to 4.2 V. The corresponding energy density calculated on the basis of the galvanostatic curves is listed in Table S3. In Figs. 6(c) and SI Fig. S10, the galvanostatic charge-discharge curves for this device at different current densities display symmetric quasitriangular shapes, indicating combination of different storage mechanisms. In brief, during the charge process, Li^+ ions react with the $cNiCo_2O_4$ nanocomposites while the PF_6^- anions are absorbed on the electrode–electrolyte interface, and the reactions are completely reversed in the discharge process with additional lithium ion adsorbed on the cathode surface. The specific capacitances of the LIC devices were calculated based on the previous work [53]. (see SI for the details) The calculated specific capacitances at different current densities are summarized in Fig. S11. The energy density and power density of the LIC devices were calculated based on the method in supplementary materials. The LIC devices in this work and several reported systems are compared in

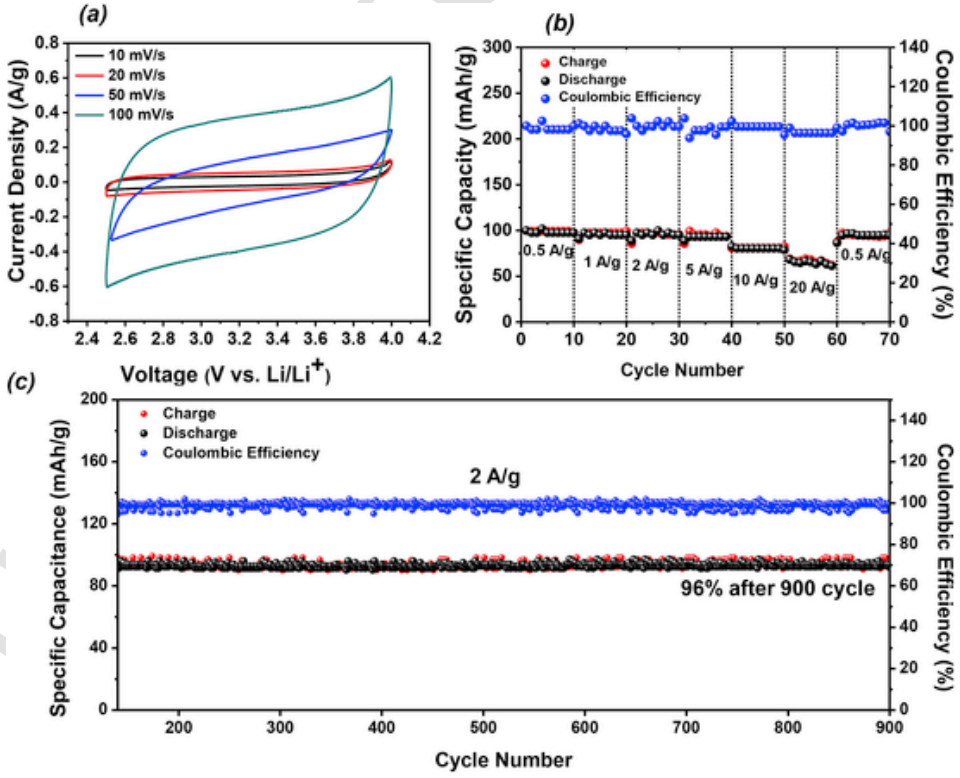

Fig. 5. Electrochemical properties of the VACNFs electrode. (a) CV curves at various scan rates from 10 mV/s to 100 mV/s. (b) Rate performance at different current densities ranging from 0.5 to 20 A/g. (c) Cyclic performance of the VACNFs cathode electrode at 2 A/g up to 900 cycles.

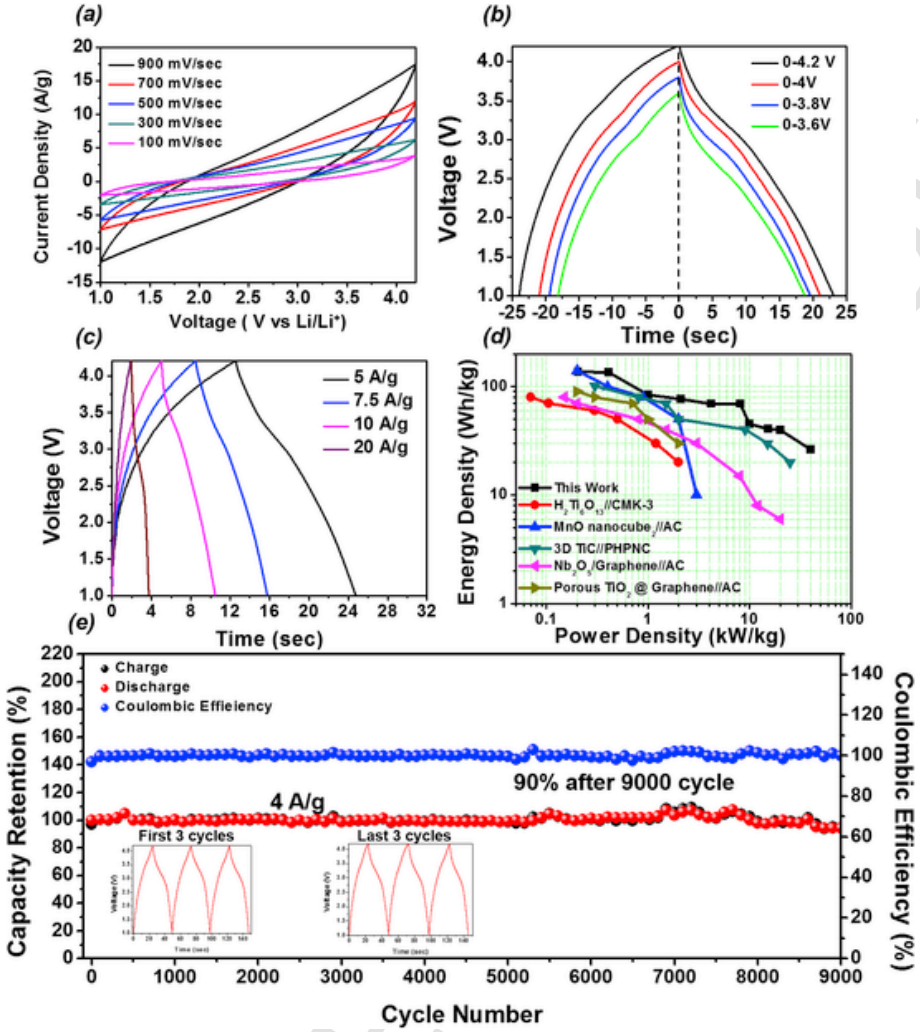

Fig. 6. Electrochemical properties of the Li-ion capacitor. (a) CV curves at various scan rates. (b) Galvanostatic charge-discharge curves at different voltage window with fixed current density of 5 A/g. (c) Galvanostatic curves of LIC under different current density ranging from 5 to 20 A/g. (d) Ragone plot of the VACNFs|c$NiCo_2O_4$ LIC with other recently published results [14,15,17,54,55]. (e) Cycling performance of the LIC with current density of 4 A/g. The insets show the galvanostatic curves for the first and last three cycles.

Ragone plot (Fig. 6 (d)). The LICs in this work can achieve a high energy density of 136.90 W h/kg (at 200 W/kg), which is among the best values reported. It is worth to mention that the applications of LICs usually require high power density (>10 kW/kg). Therefore, it is more meaningful to compare the energy densities of LICs at practically important power densities. At high power density of 40 kW/kg, under which a full charge-discharge can be finished within 4 s, the LIC in this work exhibited high energy density of 26.44 W h/kg. From Ragone plot, it is clear that the LIC in this work has significant energy density advantages over other reported systems at power density >2 kW/kg. To evaluate the cyclability of the LIC device, the long cycle experiments were conducted at a fixed current density of 4 A/g. As shown in Fig. 6(e), a capacitance retention of 90% was achieved after 9000 cycles. The inset in Fig. 6(e) shows the galvanostatic curves of the first and last three cycles in the cyclability test. It is clear that the galvanostatic curves remained unchanged, which confirmed the good cyclability of the VACNFs|c$NiCo_2O_4$ LIC. A comparison of the cyclability test with other published LIC systems is presented in Table S4 and this LIC is also among the most stable LIC systems. The good cyclability of the LIC could be attributed to the well-defined nanoporous structure of the c$NiCo_2O_4$ and VACNFs. The TEM and SEM micrographs of the nanostructure of anode and cathode after cycling were collected (SI, Fig. S12). The results showed that the original morphology of the electrode materials was preserved, indicating the robust nanostructure of the active materials. As expected, the well-preserved nanostructure suggests the stability of the kinetic balance of the LICs during cycling. It is worth to note that the materials developed in this work could be synthesized in large scale if needed. Considering the anode materials, hydrothermal reaction could be scaled up by simply enlarging the batch reaction with larger reactor. For instance, the mass production of metal oxide with hydrothermal synthesis has been demonstrated with high yield and large quantity (around 60 g per batch) [56]. For the cathode materials, it would be possible to scale up the VACNF by using fluidized bed chemical vapor deposition (FBCVD), in which system the heat and mass transfer is more efficient and enable a large contact area between the catalyst and reactant [57,58].

3.6. Kinetic analysis of LIC electrodes

To further understand the kinetic diffusion process of Li in both anode and cathode, galvanostatic intermittent titration technique (GITT) tests were conducted. As shown in Fig. 7, the lithium diffusivity as a function of the cell voltage was utilized to calculate the. Weppner and Huggins expression [59] was utilized to calculate diffusivities of the Li:

$$D_{Li} = \frac{3L^2}{\pi\tau}\left(\frac{\Delta E_s}{\Delta E_\tau}\right)^2 \quad (4)$$

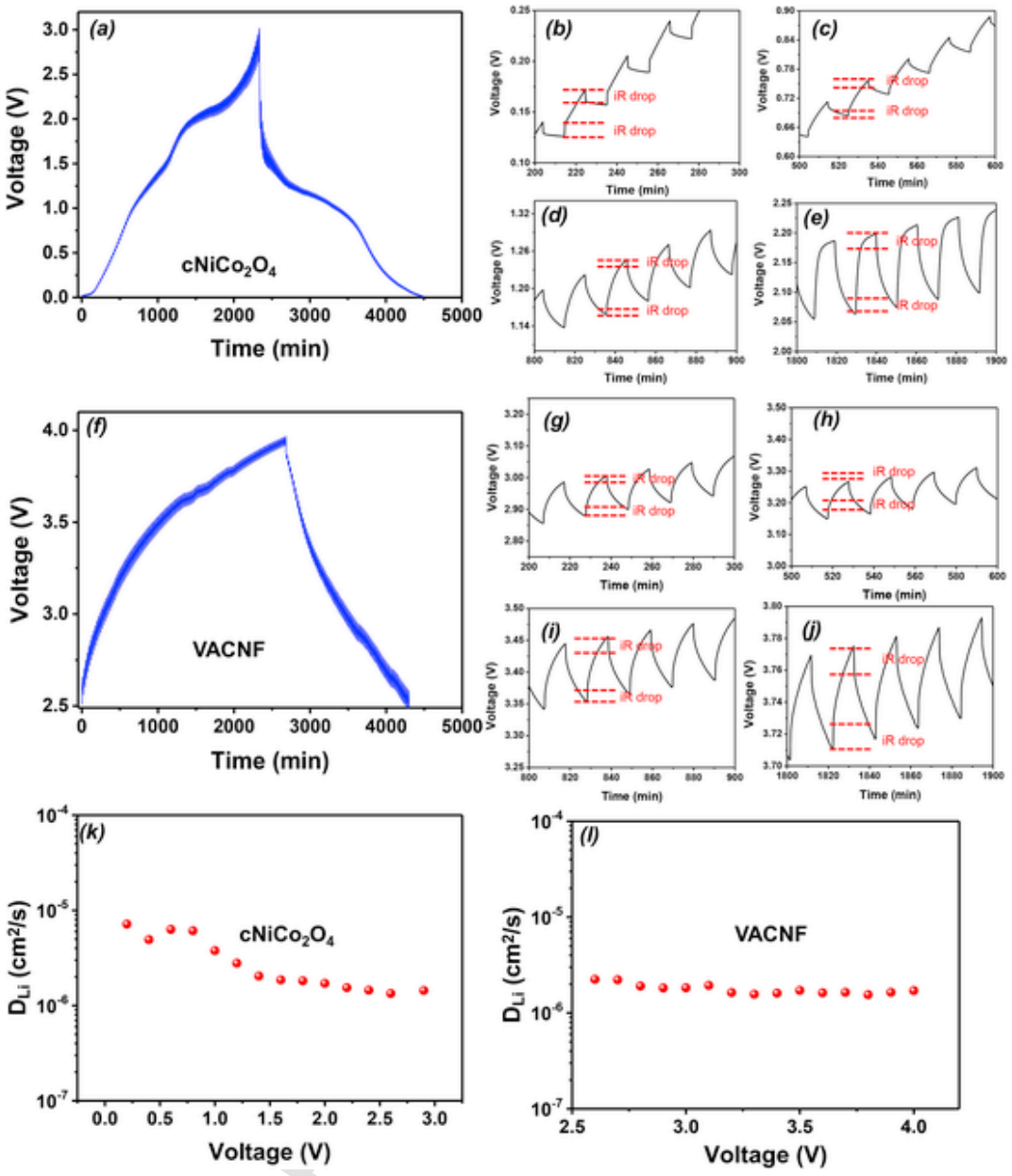

Fig. 7. Galvanostatic intermittent titration technique (GITT) analysis of electrodes (a) GITT curve of $cNiCo_2O_4$ electrode. (b–e) Enlarged profiles at four distinct points at 0.1–0.25 V (b), 0.6–0.9 V (c), 1.14–1.32 V (d) and 2.0–2.25 V (e). (f) GITT curve of VACNF electrode. (g–j) Enlarged profiles at four distinct points at 2.8–3.1 V (g), 3.1–3.3 V (h), 3.3–3.5 V (i) and 3.7–3.8 V (j). (k,l) Lithium diffusivities of the (k) $cNiCo_2O_4$ and (l) VACNF electrodes as a function of the cell potential determined by GITT profiles during charging. All voltage is vs. Li/Li^+.

where τ refers to interval time of the current pulse (600 s), L refers to the electrode thickness. ΔE_s is the steady-state voltage change due to the current pulse. ΔE_τ is the voltage change during the constant current pulse, eliminating the iR drop. Fig. 7(a) depicts the lithium diffusivities as a function of cell potential of $cNiCo_2O_4$ during the galvonostatic process. The lithium ion diffusivities of $cNiCo_2O_4$ during the charge process (Fig. 7(b–e)) was further measured at four distinct points (0.1 V, 0.7 V, 1.2 V and 2.2 V, vs. Li/Li^+) to investigate the kinetic diffusion of the Li ions in the nanostructured anode. The lithium diffusivities measured at these four points are plotted in Fig. 7(k). The obtained lithium diffusivities is between 1×10^{-6} and 8×10^{-6} cm^2/s, with higher lithium diffusivities at lower voltage. On the cathode side, the lithium (or ion) diffusivities as a function of cell potential of VACNF were studied by GITT method as well (Fig. 7(f)). The lithium ion diffusivities of VACNF were also measured at four distinct points (2.9 V, 3.2 V, 3.4 V and 3.8 V, Fig. 7(g–j)). The diffusivities of the Li in VACNF are around 2×10^{-6} cm^2/s and remain stable at different voltage (Fig. 7(l)), which is consistent with the capacitive behavior on the cathode side. In comparison, the lithium ion diffusivities measured in intercalation graphite electrode were lower than 10^{-7} cm^2/s [60–62]. Based on lithium ion diffusivities results, the kinetics between $cNiCo_2O_4$ anode and VACNF cathode matched well.

4. Conclusions

In summary, a new design of the LIC has been developed by introducing $cNiCo_2O_4$ nanocomposites from MOF derivatives as anode and highly porous VACNFs as cathode. The device was operated in a non-aqueous electrolyte to achieve well-balanced energy and power densities. The LIC devices delivered a high energy density up to 136.9 W h/kg as well as a balanced energy density of 26.44 W h/kg at high power density of 40 kW/kg (charge/discharge within 4 s). The LIC exhibited a

good cycle stability (≈90% retention after 9000 cycles) within the voltage range of 1–4.2 V. The high performance of the LIC devices can be attributed to the well-designed nanostructured materials: firstly, the well-defined nanostructural $cNiCo_2O_4$ anode possessed both high porosity and conductivity, leading to fast pseudocapacitive behavior. Secondly, the volume change in conversion reaction anode could be well-addressed with hierarchical $cNiCo_2O_4$ nanostructures, which produced excellent reversibility of the anode and the LIC device. Finally, the nanoscale dimensions of the porous carbon with vertically aligned orientation decreased the ion transport path length on the cathode and increased the amount of electrolyte ions near the surface of the positive electrode during the adsorption/desorption processes. This work demonstrated that high performance electrode for LIC device can be achieved by the rational design of materials with controlled nanostructures.

Declaration of interests

The authors declared no conflicts of interests.

Acknowledgements

The authors acknowledge Dr. B. Wang and Dr. M. Gao for the help with the SEM and TEM. The SEM observations using Quanta450 were carried out at the Liquid Crystal Institute Characterization Facility of Kent State University. This work is supported by the National Science Foundation (NSF-CBET 1706681).

Appendix A. Supplementary data

Supplementary data to this article can be found online at https://doi.org/10.1016/j.ensm.2019.07.034.

References

[1] M. Salanne, B. Rotenberg, K. Naoi, K. Kaneko, P.L. Taberna, C.P. Grey, B. Dunn, P. Simon, Efficient storage mechanisms for building better supercapacitors, Nat. Energy 1 (2016) 16070.
[2] M.F. El-Kady, Y. Shao, R.B. Kaner, Graphene for batteries, supercapacitors and beyond, Nat. Rev. Mater 1 (2016) 16033.
[3] H. Li, Y. Zhu, S. Dong, L. Shen, Z. Chen, X. Zhang, G. Yu, Self-assembled Nb_2O_5 nanosheets for high Energy–High power sodium ion capacitors, Chem. Mater. 28 (2016) 5753–5760.
[4] H. Li, L. Peng, Y. Zhu, X. Zhang, G. Yu, Achieving high-energy-high-power density in a flexible quasi-solid-state sodium ion capacitor, Nano Lett. 16 (2016) 5938–5943.
[5] K. Naoi, S. Ishimoto, J. Miyamoto, W. Naoi, Second generation 'nanohybrid supercapacitor': evolution of capacitive energy storage devices, Energy Environ. Sci. 5 (2012) 9363–9367.
[6] V. Aravindan, J. Gnanaraj, Y.S. Lee, S. Madhavi, Insertion-Type Electrodes for Nonaqueous Li-Ion Capacitors, Chem. Rev. 23 (2014) 11619–11635.
[7] J. Luo, J. Liu, Z. Zeng, C.F. Ng, L. Ma, H. Zhang, J. Lin, Z. Shen, H.J. Fan, Three-dimensional graphene foam supported Fe_3O_4 lithium battery anodes with long cycle life and high rate capability, Nano Lett. 13 (2013) 6136–6143.
[8] Y. Zhou, X. Rui, W. Sun, Z. Xu, Y. Zhou, W.J. Ng, Q. Yan, E. Fong, Biochemistry-enabled 3D foams for ultrafast battery cathodes, ACS Nano. 9 (2015) 4628–4635.
[9] Z. Niu, J. Chen, H.H. Hng, J. Ma, X. Chen, A leavening strategy to prepare reduced graphene oxide foams, Adv. Mater. 24 (2012) 4144–4150.
[10] Z.-S. Wu, Y. Sun, Y.-Z. Tan, S. Yang, X. Feng, K. Müllen, Three-dimensional graphene-based macro- and mesoporous frameworks for high-performance electrochemical capacitive energy storage, J. Am. Chem. Soc. 134 (2012) 19532–19535.
[11] M. Armand, J.M. Tarascon, Building better batteries, Nature 451 (2008) 652–657.
[12] V. Augustyn, P. Simon, B. Dunn, Pseudocapacitive oxide materials for high-rate electrochemical energy storage, Energy Environ. Sci. 7 (2014) 1597–1614.
[13] L. Shen, H. Lv, S. Chen, P. Kopold, P.A. Aken, X. Wu, J. Maier, Y. Yu, Pea-pod-like Li_3VO_4/N-doped carbon nanowires with pseudocapacitive properties as advanced materials for high-energy lithium-ion capacitors, Adv. Mater. 29 (2017) 1700142.
[14] R. Wang, S. Wang, D. Jin, Y. Zhang, Y. Cai, J. Ma, L. Zhang, Engineering layer structure of MoS_2-graphene composites with robust and fast lithium storage for high-performance Li-ion capacitors, Energy Storage Mater 9 (2017) 195–205.
[15] J. Niu, R. Shao, M. Liu, J. Liang, Z. Zhang, M. Dou, Y. Huang, F. Wang, Dual phase enhanced superior electrochemical performance of nanoporous bismuth-tin alloy anodes for magnesium-ion batteries, Energy Storage Mater 12 (2018) 145–152.
[16] L. Kong, C. Zhang, J. Wang, W. Qiao, L. Ling, D. Long, Free-standing *T*-Nb_2O_5/graphene composite papers with ultrahigh gravimetric/volumetric capacitance for Li-ion intercalation pseudocapacitor, ACS Nano 9 (2015) 11200–11208.
[17] J. Luo, W. Zhang, H. Yuan, C. Jin, L. Zhang, H. Huang, C. Liang, Y. Xia, J. Zhang, Y. Gan, X. Tao, Pillared structure design of MXene with ultralarge interlayer spacing for high-performance lithium-ion capacitors, ACS Nano 11 (2017) 2459–2469.
[18] R.V. Salvatierra, D. Zakhidov, J. Sha, N.D. Kim, S.-K. Lee, A.-R.O. Raji, N. Zhao, J.M. Tour, Graphene carbon nanotube carpets grown using binary catalysts for high-performance lithium-ion capacitors, ACS Nano 11 (2017) 2724–2733.
[19] H. Wang, Y. Zhang, H. Ang, Y. Zhang, H.T. Tan, Y. Zhang, Y. Guo, J.B. Franklin, X.L. Wu, M. Srinivasan, H.J. Fan, Q. Yan, A high-energy lithium-ion capacitor by integration of a 3D interconnected titanium carbide nanoparticle chain anode with a pyridine-derived porous nitrogen-doped carbon cathode, Adv. Funct. Mater. 26 (2016) 3082–3093.
[20] N. Arun, A. Jain, V. Aravindan, S. Jayaraman, W.C. Ling, M.P. Srinivasan, S. Madhavi, Nanostructured spinel $LiNi_{0.5}Mn_{1.5}O_4$ as new insertion anode for advanced Li-ion capacitors with high power capability, Nano Energy 12 (2015) 69–75.
[21] J. Ding, Z. Li, K. Cui, S. Boyer, D. Karpuzov, D. Mitlin, Heteroatom enhanced sodium ion capacity and rate capability in a hydrogel derived carbon give record performance in a hybrid ion capacitor, Nano Energy 23 (2016) 129–137.
[22] C. Liu, C. Zhang, H. Fu, X. Nan, G. Cao, Exploiting high-performance anode through tuning the character of chemical bonds for Li-ion batteries and capacitors, Adv. Energy Mater 7 (2017) 1601127.
[23] A. Chaturvedi, P. Hu, V. Aravindan, C. Kloc, S. Madhavi, Unveiling two-dimensional TiS_2 as an insertion host for the construction of high energy Li-ion capacitors, J. Mater. Chem. A 25 (2017) 9177–9181.
[24] H. Wang, C. Guan, X. Wang, H.J. Fan, A high energy and power Li-ion capacitor based on a TiO_2 nanobelt array anode and a graphene hydrogel cathode, Small 11 (2015) 1470–1477.
[25] Y. Ma, H. Chang, M. Zhang, Y. Chen, Graphene-based materials for lithium-ion hybrid supercapacitors, Adv. Mater. 27 (2015) 5296–5308.
[26] X. Yang, H. Niu, H. Jiang, Q. Wang, F. Qu, A high energy density all-solid-state asymmetric supercapacitor based on MoS_2/graphene nanosheets and MnO_2/graphene hybrid electrodes, J. Mater. Chem. A 4 (2016) 11264–11275.
[27] H. Kim, M.Y. Cho, M.H. Kim, K.Y. Park, H. Gwon, Y. Lee, K.C. Roh, K. Kang, A novel high-energy hybrid supercapacitor with an anatase TiO_2–reduced graphene oxide anode and an activated carbon cathode, Adv. Energy Mater. 3 (2013) 1500–1506.
[28] R. Wang, J. Lang, P. Zhang, Z. Lin, X. Yan, Fast and large lithium storage in 3D porous VN nanowires–graphene composite as a superior anode toward high-performance hybrid supercapacitors, Adv. Funct. Mater. 25 (2015) 2270–2278.

[29] S. Zhang, C. Li, X. Zhang, X. Sun, K. Wang, Y. Ma, High performance lithium-ion hybrid capacitors employing Fe_3O_4–graphene composite anode and activated carbon cathode, ACS Appl. Mater. Interfaces 9 (2017) 17136–17144.
[30] K. Xie, X. Qin, X. Wan, Y. Wang, H. Tao, Q. Wu, L. Yang, Z. Hu, Carbon nanocages as supercapacitor electrode materials, Adv. Mater. 24 (2012) 347–352.
[31] H. Wang, H.T. Tan, H. Yi, Y. Zhang, G. Guo, X. Wang, S. Madhavi, Q. Yan, Integrating three-dimensional graphene/Fe_3O_4@C composite and mesoporous Co(OH)2 nanosheets arrays/graphene foam into a superior asymmetric electrochemical capacitor, RSC Adv. 5 (2015) 88191.
[32] F. Zou, Y.M. Chen, K. Liu, Z. Yu, W. Liang, S.M. Bhaway, M. Gao, Y. Zhu, Metal organic frameworks derived hierarchical hollow NiO/Ni/graphene composites for lithium and sodium storage, ACS Nano 10 (2016) 377–386.
[33] W. Guo, W. Sun, Y. Wang, Multilayer CuO@NiO hollow spheres: microwave-assisted metal–organic-framework derivation and highly reversible structure-matched stepwise lithium storage, ACS Nano 9 (2015) 11462–11471.
[34] K. Liu, F. Zou, Y. Sun, Z. Yu, X. Liu, L. Zhou, Y. Xia, B.D. Vogt, Y. Zhu, Self-assembled Mn_3O_4/C nanospheres as high-performance anode materials for lithium ion batteries, J. Power Sources 395 (2018) 92–97.
[35] S. Peng, L. Zhang, C. Zhang, Y. Ding, X. Guo, G. He, G. Yu, Gradient-distributed metal–organic framework–based porous membranes for nonaqueous redox flow batteries, Adv. Energy Mater. 8 (2018) 1802533.
[36] Y. Liu, Z. Wang, Y. Zhong, M. Tade, W. Zhou, Z. Shao, Design of hierarchical Ni-Co@Ni-Co layered double hydroxide core-shell structured nanotube Array for high-performance flexible all-solid-state battery-type supercapacitors, Adv. Funct. Mater. 27 (2017) 1605307.
[37] D.Y. Lee, S.J. Yoon, N.K. Shrestha, S.H. Lee, H. Ahn, S.H. Han, Unusual energy storage and charge retention in Co-based metal–organic-frameworks, Microporous Mesoporous Mater. 153 (2012) 163–165.
[38] J. Zhang, H. Hu, Z. Li, X.W. Lou, Double-shelled nanocages with cobalt hydroxide inner shell and layered double hydroxides outer shell as high-efficiency polysulfide mediator for lithium-sulfur batteries, Angew. Chem. Int. Ed. 55 (2016) 3982.
[39] M. Sathiya, A.S. Prakash, K. Ramesha, J.M. Tarascon, A.K. Shukla, V_2O_5-Anchored carbon nanotubes for enhanced electrochemical energy storage, J. Am. Chem. Soc. 133 (2011) 16291–16299.
[40] P. Simon, Y. Gogotsi, B. Dunn, Where do batteries end and supercapacitors begin?, Science 343 (2014) 1210–1211.
[41] X. Sun, W. Si, X. Liu, J. Deng, L. Xi, L. Liu, C. Yan, O.G. Schmidt, Multifunctional Ni/NiO hybrid nanomembranes as anode materials for high-rate Li-ion batteries, Nano Energy 9 (2014) 168–175.
[42] G. Huang, X. Guo, X. Cao, Q. Tian, H. Sun, 3D network single-phase $Ni_{0.9}Zn_{0.1}O$ as anode materials for lithium-ion batteries, Nano Energy 28 (2016) 338–345.
[43] B. Yan, M. Li, X. Li, Z. Bai, L. Dong, D. Li, Electrochemical impedance spectroscopy illuminating performance evolution of porous core–shell structured nickel/nickel oxide anode materials, Electrochim. Acta. 164 (2015) 55–61.
[44] H. Li, Y. Tao, X. Zheng, J. Luo, F. Kang, H.-M. Cheng, Q.-H. Yang, Ultra-thick graphene bulk supercapacitor electrodes for compact energy storage, Energy Environ. Sci. 9 (2016) 3135–3142.
[45] D. Xie, X. Xia, Y. Zhong, Y. Wang, D. Wang, X. Wang, J. Tu, Exploring advanced sandwiched arrays by vertical graphene and N-doped carbon for enhanced sodium storage, Adv. Energy Mater. 7 (2017) 1601804.
[46] J.-J. Shao, W. Lv, Q.-H. Yang, Self-assembly of graphene oxide at interfaces, Adv. Mater. 26 (2014) 5586–5612.
[47] J. Yang, C. Yu, X. Fan, S. Liang, S. Li, H. Huang, Z. Ling, C. Hao, J. Qiu, Electroactive edge site-enriched nickel–cobalt sulfide into graphene frameworks for high-performance asymmetric supercapacitors, Energy Environ. Sci. 9 (2016) 1299–1307.
[48] M. Cai, R.A. Outlaw, R.A. Quinlan, D. Premathilake, S.M. Butler, J.R. Miller, Fast response, vertically oriented graphene nanosheet electric double layer capacitors synthesized from C_2H_2, ACS Nano 8 (2014) 5873–5882.
[49] A.C. Ferrari, Raman spectroscopy of graphene and graphite: disorder, electron–phonon coupling, doping and nonadiabatic effects, Solid State Commun. 143 (2007) 47–57.
[50] A. Banerjee, K.K. Upadhyay, D. Puthusseri, V. Aravindan, S. Madhavi, S. Ogale, MOF-derived crumpled-sheet-assembled perforated carbon cuboids as highly effective cathode active materials for ultra-high energy density Li-ion hybrid electrochemical capacitors (Li-HECs), Nanoscale 6 (2014) 4387–4394.
[51] V. Aravindan, D. Mhamane, W.C. Ling, S. Ogale, S. Madhavi, Nonaqueous lithium-ion capacitors with high energy densities using trigol-reduced graphene oxide nanosheets as cathode-active material, ChemSusChem 6 (2013) 2240–2244.
[52] X. Zhao, C.M. Hayner, M.C. Kung, H.H. Kung, Flexible holey graphene paper electrodes with enhanced rate capability for energy storage applications, ACS Nano 5 (2011) 8739–8749.
[53] J. Ding, H. Wang, Z. Li, K. Cui, D. Karpuzov, X. Tan, A. Kohandehghan, D. Mitlin, Peanut shell hybrid sodium ion capacitor with extreme energy–power rivals lithium ion capacitors, Energy Environ. Sci. 8 (2015) 941–955.
[54] C. Liu, C. Zhang, H. Song, C. Zhang, Y. Liu, X. Nan, G. Cao, Mesocrystal MnO cubes as anode for Li-ion capacitors, Nano Energy 22 (2016) 290–300.
[55] F. Wang, C. Wang, Y. Zhao, Z. Liu, Z. Chang, L. Fu, Y. Zhu, Y. Wu, D. Zhao, A quasi-solid-state Li-ion capacitor based on porous TiO_2 hollow microspheres wrapped with graphene nanosheets, Small 12 (2016) 6207–6213.
[56] S. Ghasaban, M. Atai, M. Imani, Simple mass production of zinc oxide nanostructures via low-temperature hydrothermal synthesis, Mater. Res. Express 4 (2017) 35010.
[57] C. Vahlas, B. Caussatb, P. Serp, G.N. Angelopoulos, Principles and applications of CVD Powder Technology, Mater. Sci. Eng. R. 53 (2006) 1–72.
[58] F. Danafar, A. Fakhru'l-Razi, A. Salleh, D. Radiah, Fluidized bed catalytic chemical vapor deposition synthesis of carbon nanotubes - a review, Chem. Eng. J. 155 (2009) 37–48.
[59] W. Weppner, R.A. Huggins, Determination of the kinetic parameters of mixed-conducting electrodes and application to the system Li_3Sb, J. Electrochem. Soc. 124 (1977) 1569–1578.
[60] Y. Wu, M.V. Reddy, B.V.R. Chowdari, S. Ramakrishna, Long-term cycling studies on electrospun carbon nanofibers as anode material for lithium ion batteries, ACS Appl. Mater. Inter. 5 (2013) 12175–12184.
[61] P. Verma, P. Maire, P. Novak, A review of the features and analyses of the solid electrolyte interphase in Li-ion batteries, Electrochim. Acta. 55 (2010) 6332–6341.
[62] E. Markevich, M.D. Levi, D. Aurbach, Comparison between potentiostatic and galvanostatic intermittent titration techniques for determination of chemical diffusion coefficients in ion-insertion electrodes, J. Electroanal. Chem. 580 (2005) 231–237.